

Wavefront Sensing and the Active Optics System of the Dark Energy Camera.

Aaron Roodman, Kevin Reil, Chris Davis

Kavli Institute for Particle Astrophysics & Cosmology
SLAC National Accelerator Laboratory
Stanford University, Menlo Park CA, USA

ABSTRACT

Wavefront sensing and the Active Optics System (AOS) of the Dark Energy Camera (DECam) at the CTIO 4-meter Blanco telescope are described. DECam utilizes four pairs of intra/extra-focal CCDs located on the edge of the focal plane for wavefront sensing. Out-of-focus stars are selected, individually fit to a pupil plane Zernike expansion and then collectively analyzed in the time between exposures. The AOS uses this information to control the prime-focus camera's five degrees of freedom. The AOS is now in routine use, operating with unsupervised control of the focus and camera alignment, both for the Dark Energy Survey and community observing. The design, commissioning and operation of the AOS along with results from the wavefront measurements are described. In particular, wavefront measurements of the complete optical system, including primary mirror aberrations, are shown. Lastly, preliminary results using these wavefront measurements to model the DECam point spread function are presented.

Keywords: DECam, DES, Active Optics, Wavefront Sensors, Curvature Sensors, Donuts

1. INTRODUCTION

The Dark Energy Camera (DECam)¹ is a 3 square-degree field-of-view imager built for the Dark Energy Survey (DES),² and now in operation on the CTIO Blanco 4-meter telescope. DES is a 5000 square degree optical survey designed to study dark energy through multiple probes: weak lensing, galaxy clusters, supernova, strong lensing and large scale structure. This scientific program requires excellent image quality and so DECam was designed with focus-diversity wavefront sensors placed on the same focal plane as the 62 science sensors, and a prime-focus hexapod to allow rapid adjustment of the camera's focus and alignment with respect to the primary. This paper describes the Active Optics System (AOS) which maintains unsupervised control of DECam's focus and alignment. The AOS utilizes eight 2k by 2k CCDs (wavefront sensors) located on the edge of the DECam field of view and placed out-of-focus by $\pm 1.5\text{mm}$, as shown in Figure 1. We present in this proceedings details on both the design of the AOS and its operation during the commissioning and science verification of DECam and first year of DES operations. Prior to the commissioning of DECam, substantial testing of the wavefront retrieval algorithm was performed using images taken with the Blanco telescope's previous prime focus camera^{3,4}

2. DECAM ACTIVE OPTICS SYSTEM

The AOS consists of several software modules, acting in concert, which implement the following steps: 1) receive the eight $2k \times 2k$ wavefront CCD images from the DECam data acquisition, 2) locate usable donuts by finding contiguous pixels which have local flux maxima and satisfy total flux, size and shape requirements, 3) distribute small cut-out images of the donuts to processing farm nodes, 4) run the wavefront retrieval algorithm on this ensemble of donuts, 5) collect the fitted Zernike coefficients and distill them into DECam focus and hexapod alignment displacements, 6) pass these values into a PID control loop for each of the five degrees of freedom (focus, x and y decenter, tip and tilt) and hence 7) produce hexapod adjustments to be applied prior to the next image. All steps are performed in a 7 second time window between the time when the wavefront CCDs are

Further author information:

E-mail: roodman@slac.stanford.edu, Telephone: 1 650 926 2705

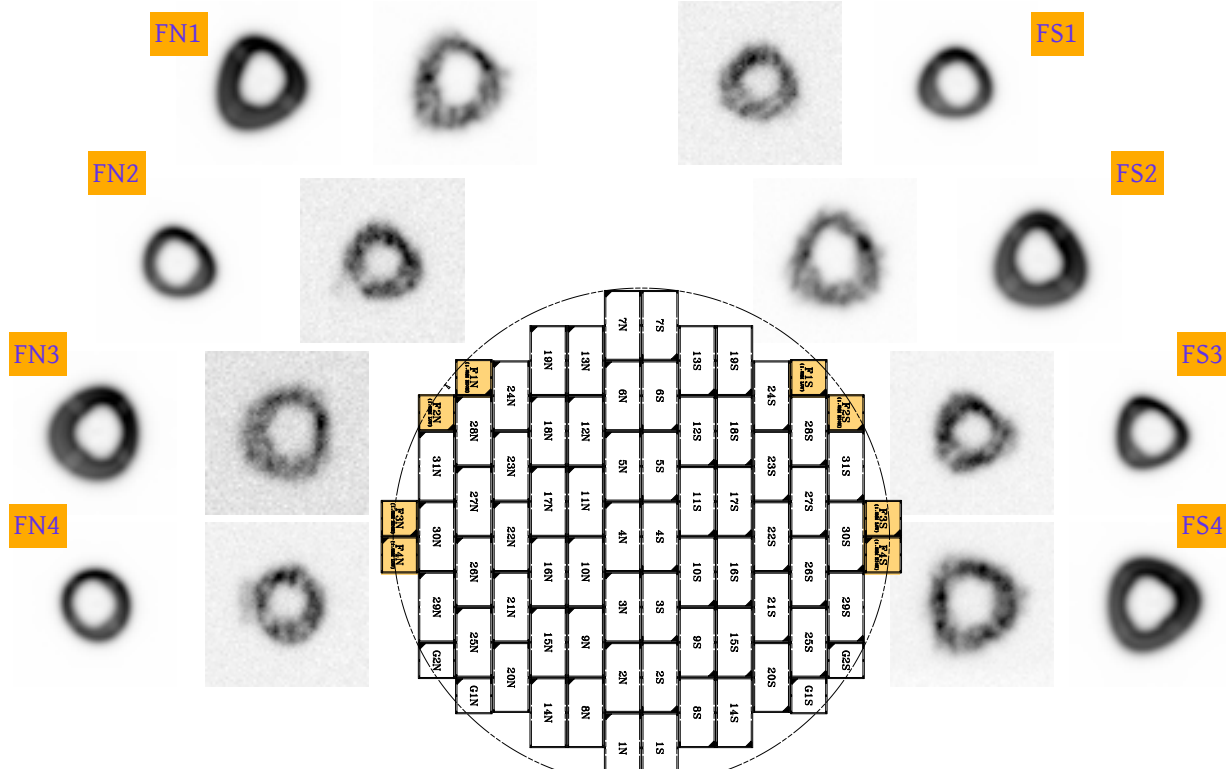


Figure 1. The DECam focal plane, with the 8 wavefront sensors shown and an example out-of-focus star from each, along with the corresponding fitted model. These donuts come from an image taken during DECam commissioning; the camera was roughly $200\mu\text{m}$ out of focus at the time.

read-out and the start of the next image. Since the DECam science CCDs are $2k \times 4k$ and so take double the time to read-out, the AOS operates with no extra downtime. A block diagram of the AOS is shown in Figure 2. On average 30 donuts are analyzed per image, with at least 10 donuts available 97% of the time. The wavefront analysis and the determination of the hexapod alignment is described in Section 5. An identical analysis is repeated offline, except that offline we use *sextractor*⁵ to locate donuts and can afford to use a looser selection requirement; with no time-limits between 10-500 donuts are located, fit and analyzed per image.

The DECam hexapod position is commanded from two sources: a fixed look-up-table (LUT) and the AOS. The LUT contains static focus and alignment settings indexed by telescope orientation, hour angle and declination, and in the case of focus only also by filter. The LUT values were determined from a suit of engineering images, collected with the entire focal plane out of focus, and covering a grid of points in altitude and azimuth. The LUT's are described in more detail in Section 5.3. In the time between images, the LUT hexapod settings are applied as appropriate for the following image and then the AOS adjustments are also applied, adding to the LUT values. We find that deviations from the LUT values do accumulate over time, and so the AOS adjustments are continually updated throughout each night of observing.

3. WAVEFRONT RETRIEVAL ALGORITHM

We extract wavefront information from out-of-focus stars (donuts) with a forward-modeling non-linear χ^2 fit. Although we image both sides of focus in adjacent CCDs, we choose to use a forward model^{6,7} instead of using the transport-of-intensity approach⁸ because forward modeling allows us to also easily extract wavefronts from a single donut and to directly account for DECam's very complicated pupil shape.

Our algorithm (*donutengine*) models the image in terms of a pupil-plane Zernike decomposition, using the

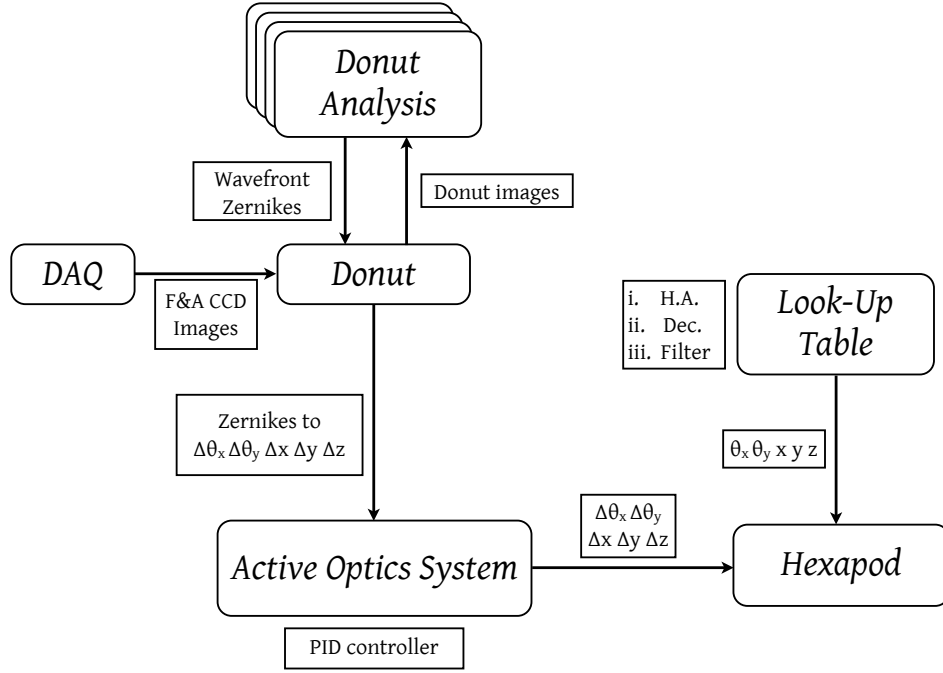


Figure 2. Block diagram of the AOS

Fraunhofer diffraction integral:

$$I(x, y) \sim \left| \mathcal{F} \left\{ P(\rho, \theta) e^{2\pi i W(\rho, \theta)/\lambda} \right\} \right|^2 \quad (1)$$

The pupil function, $P(\rho, \theta)$, is described by a model of the apertures that contribute to the central obscuration of the pupil, as a function of the position on the focal plane. These surfaces include: the top end of DECam, the filter-exchange box which extends into the aperture, the bottom end of DECam and the Blanco primary mirror's cassegrain baffle. On axis, these apertures all line up, but off axis they separately contribute to the obscuration. In addition, the large field-of-view produces a large variation in the obscuration as seen across the focal plane. Our model for the obscuration accounts for the size, shape and location on the optical axis of each contributing aperture. A star taken 12mm out-of-focus, in Figure 3, illustrates this complicated pupil shape.

Next the wavefront $W(\rho, \theta)$ is modeled as a sum of Zernike polynomials:

$$W(\rho, \theta) = \sum_i a_i Z_i(\rho, \theta) \quad (2)$$

where the coefficients a_i of the Zernike terms are the free parameters in the fit. Note that we use a fixed value of $\lambda = 700nm$ and the Zernike numbering and normalization convention shown in Table 1. Finally the image model is convoluted with a Kolmogorov kernel to describe atmospheric seeing, characterized by Fried's parameter, and with a pixelization kernel.

While a 512×512 grid is the minimum needed to perform the FFTs in the Fraunhofer integral for images defocused by 1.5mm given our F/2.9 system, to speed up the computations we use a 256×256 grid and scale all Zernike coefficients by a compensating factor of two. This is equivalent to scaling the wavelength used by a factor of two, and for ground-based imaging there is essentially no sensitivity of donuts on wavelength. This procedure was found to give consistent results, with a factor of four improvement in cpu time compared to higher dimension grids. DECam has pixels of $15\mu m$ a plate scale of $0.27''/pixel$ and the median seeing is $0.7''$ FWHM. The 1.5mm defocus is equivalent to 8.7λ of focus aberration at 700nm, yielding donuts of roughly 40 pixels

Table 1. Zernike polynomials, as defined by Noll.⁹

Index	Name	Zernike Polynomial
2	Tilt X	$2\rho \cos \theta$
3	Tilt Y	$2\rho \sin \theta$
4	Focus	$\sqrt{3}(2\rho^2 - 1)$
5	Astigmatism Y	$\sqrt{6}\rho^2 \sin 2\theta$
6	Astigmatism X	$\sqrt{6}\rho^2 \cos 2\theta$
7	Coma Y	$\sqrt{8}(3\rho^3 - 2\rho) \sin \theta$
8	Coma X	$\sqrt{8}(3\rho^3 - 2\rho) \cos \theta$
9	Trefoil Y	$\sqrt{8}\rho^3 \sin 3\theta$
10	Trefoil X	$\sqrt{8}\rho^3 \cos 3\theta$
11	Spherical	$\sqrt{5}(6\rho^4 - 6\rho^2 + 1)$

diameter. The ratio of the size of the donuts to the seeing disk implies that there is enough wavefront sampling for of order 100 Zernike terms. Thus, although our donut images under-sample the pupil, the information they contain is more than adequate to determine the low-order Zernike terms needed for the AOS. A χ^2 is formed by comparing the image and the model summing over a postage stamp of 64 by 64 pixels, with per-pixel errors calculated from the square-root of the number of counts. The image model is completed with parameters for the total donut flux and a uniform sky background. To compare the FFT grid used in the model with the images, we take every 4th grid point. We calculate the derivative of the χ^2 with respect to the Zernike coefficients in closed form using the method described by Fienup,⁶ generalizing to include the seeing and pixelization kernels. The fit is minimized using the MIGRAD algorithm in the MINUIT¹⁰ package, which implements a Davidon-Fletcher-Powell variable-metric method. The *donutengine* algorithm is implemented in a mixture of python and C++, and the typical fitting time per donut is 0.6 seconds.

In the AOS, donut fits determine nine free Zernike coefficients: two for wavefront tilt (Z_2, Z_3), one focus (Z_4), two astigmatism (Z_5, Z_6), two coma (Z_7, Z_8) and two trefoil (Z_9, Z_{10}). Although the trefoil coefficients are not used in the AOS, there is a significant trefoil contribution in the Blanco plus DECam optical system on the edge of the field, which makes our donuts triangular in shape, so trefoil must be included in our wavefront fit. The spherical aberration (Z_{11}) term is fixed to a value taken from the Zemax model of the Blanco plus DECam¹¹ and the Fried parameter is fixed to $r_0 = 0.125$, a typical value. The fits are found to be insensitive on average to the value of r_0 while the spherical aberrations are stable over time. Fixing these parameters significantly improves the speed and stability of the computations. Note that the donut fits are repeated offline, using the same algorithm but allowing both the spherical aberration term and r_0 to float in the fit; the results are extremely similar to those from the online AOS fits. Additional fits have been performed with more Zernike terms floating, again with consistent results. The donuts have high spatial-order structure, stable in time, which would require hundreds of Zernike terms to model, as can be seen in Figure 1. The repeatability, stability and precision of the wavefront fits will be described in Section 6.

4. DECAM WAVEFRONT

We characterize the DECam wavefront by analyzing an ensemble of donuts, at the wavefront sensors for normal science images and at the science sensors from engineering images where the entire focal plane has been moved out of focus. By finding and fitting donuts covering the focal plane, we produce a map of the wavefront $W(\rho, \theta)[x, y]$ which is also a function of the focal plane coordinates x, y . Our description of the wavefront remains in terms of the Zernike coefficients, a_i , so the map consists of the values of the coefficients as a function of focal plane coordinate. A high statistics version of the wavefront map, for Zernike coefficients from focus through trefoil is shown in Figure 4 and 5. For the science sensors, these maps were formed from many images, where successive

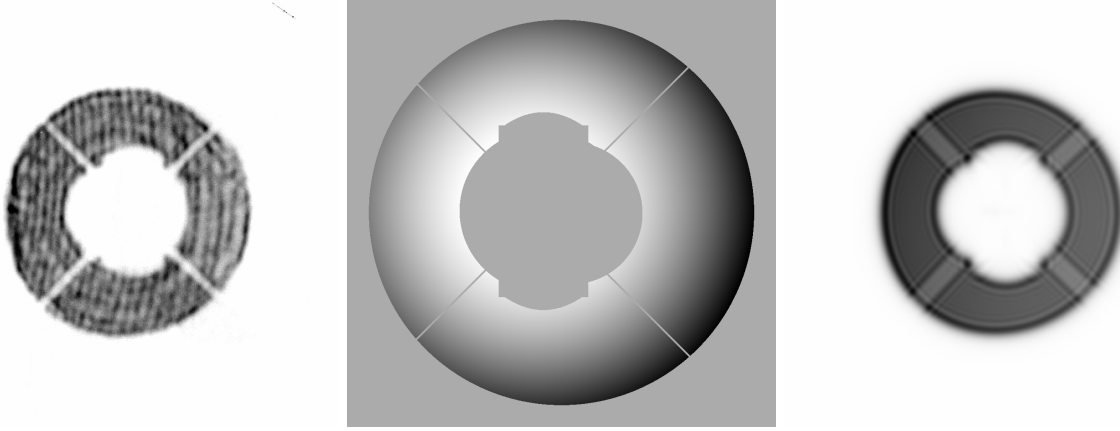


Figure 3. a) An out-of-focus star taken 12mm extra-focally, located in one of the wavefront sensors, b) The *donutengine* model of the pupil, showing the complicated DECcam shadow, c) The fitted model of the donut image.

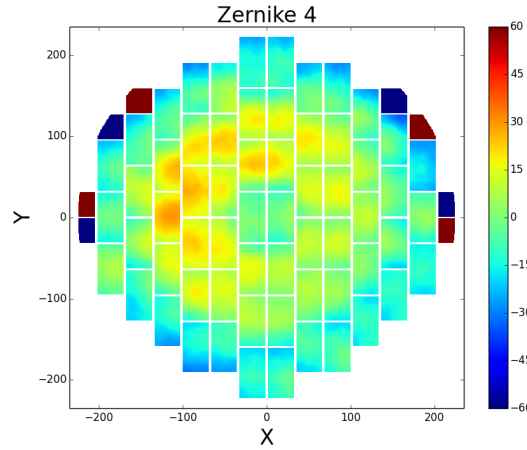


Figure 4. Wavefront map of Zernike Coefficients vs. x, y focal plane coordinates for the focus Zernike term. The color scale is in units of μm . The wavefront sensors have values at the limits of the color scale, corresponding to $\pm 1500 \mu m$.

images were combined by adjusting the values by an overall offset and slope in x, y to account for image-to-image changes in either the primary mirror aberration or DECcam alignment. In addition, the wavefront was adjusted, again by an overall offset and slope in x, y , to produce an optimal wavefront. The Zernike coefficients in the wavefront sensors were then adjusted to yield spatial continuity in the values from the adjacent science CCDs. The resulting wavefront map represents the optical performance of the combined Blanco plus DECcam system, for the ideal case of perfect DECcam alignment and primary mirror figure. The wavefront maps are seen to be extremely stable, with essentially identical behavior over a period of a year. The wavefront in r, i, z and Y band is observed to be quite similar; the wavefront maps shown here are from 30 second r band images. These wavefront maps indicate that the intrinsic wavefront has rather small aberrations over the entire DECcam focal plane, with levels well below 0.5λ over almost all of the focal plane. This excellent optical performance is borne out by the delivered image quality of DECcam; the very best images have a FWHM of $0.7''$. Note that there is a very symmetric trefoil aberration on the edges of the focal plane; the measured trefoil does have the expected magnitude and symmetry pattern from the optical prescription.

We use similar wavefront maps in the AOS, as described below. However, the maps used in the AOS and in the production of the alignment look-up-tables (LUT) were made with lower statistics, from single images, and with a preliminary version of the adjustment procedure described above. In particular the wavefront map

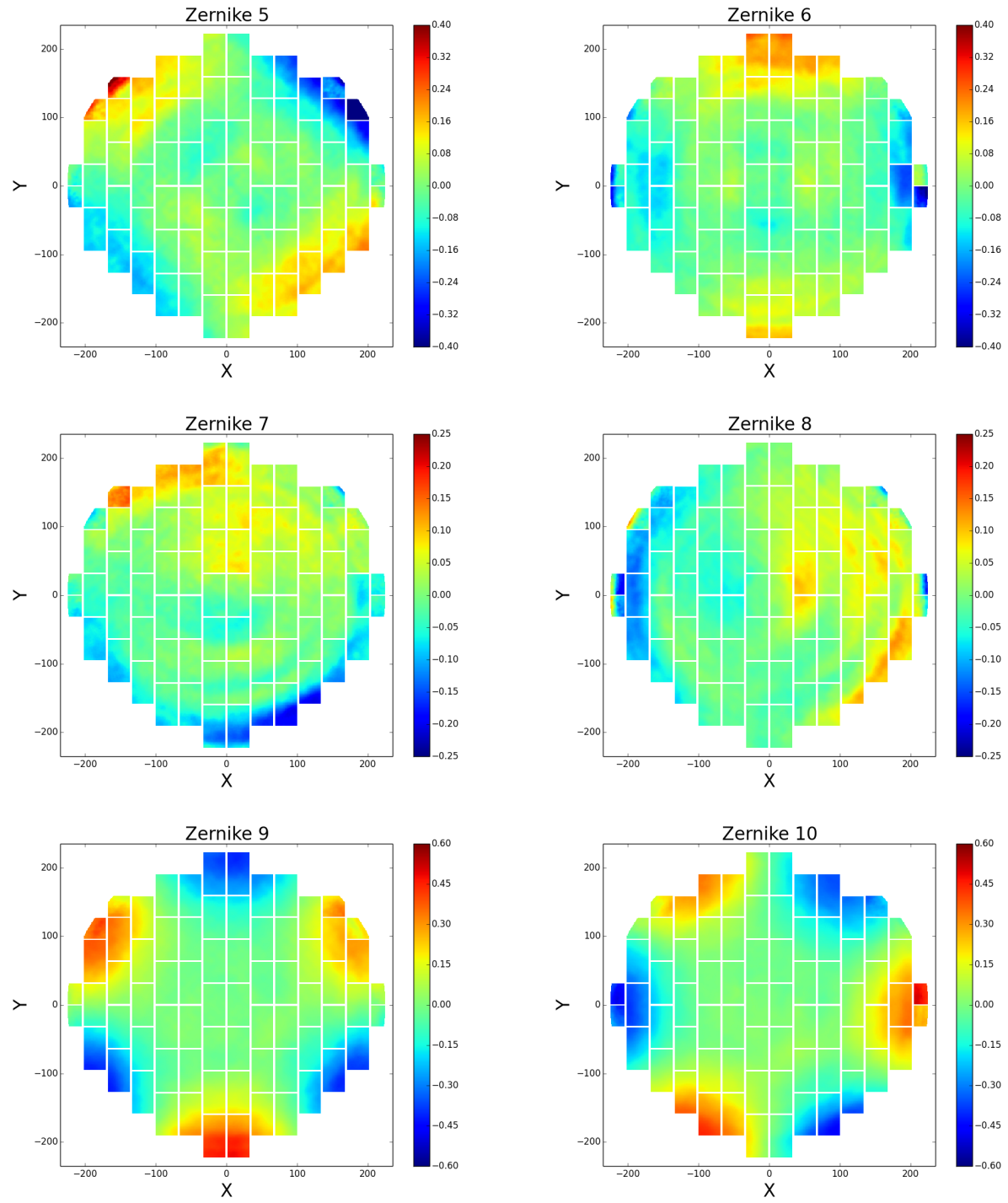


Figure 5. Wavefront maps of Zernike Coefficients vs. x, y focal plane coordinates for Zernike terms 5 through 10. The color scale is in units of λ .

for the wavefront sensors used online in the AOS was taken from a single commissioning image with good image quality. Also, it must be noted that in some cases the Zernike coefficients vary rapidly at the edges of the focal plane, especially in the wavefront sensors. This appears to be due to the fact that the donuts at the wavefront sensors show evidence for a feature where some of the flux appears outside the expected pupil outline. This can be observed by inspection of the donut in the FN4 sensor shown in Figure 1, where there is a faint distribution of flux outside the expected pupil envelope at 9 o'clock. This feature is only observed in the wavefront sensors, and appears more prevalent at higher focal plane radii, but the exact source of this effect is not currently known.

5. FOCUS AND ALIGNMENT

5.1 Wavefront Analysis

The fitted wavefronts from the eight wavefront CCDs for each image are analyzed to determine the DECam focus and relative alignment. Focus information comes solely from the focus Zernike, Z_4 , and the value of its coefficient is linearly dependent on distance from focus. In the online AOS the median value of a_4 is calculated separately from the intra-focal and extra-focal CCDs, and the distance from perfect focus is then given by $\Delta z = 172[\mu\text{m}/\lambda] \times (\langle a_4 \rangle_{\text{extra}} - \langle a_4 \rangle_{\text{intra}})$. The heights of the wavefront CCDs were accurately placed to bracket the location of the focal plane. In practice we have found that no extra adjustment of best focus is necessary.

The DECam alignment vector $\vec{h} = (\Delta X, \Delta Y, \theta X, \theta Y)$ is determined from measurements of the astigmatism and coma in the wavefront CCDs. A decenter $(\Delta X, \Delta Y)$ of DECam relative to the primary mirror produces uniform changes in coma across the focal plane, while tilts $(\theta X, \theta Y)$ produce a slope of the astigmatism across the focal plane as well as a uniform change in coma. An important feature of our method is to explicitly measure the nominal coma and astigmatism across the focal plane, as opposed to assuming a simple functional form for these aberrations. Information from the eight wavefront CCDs are combined by comparing the measured Zernike coefficient, for each aberration, against the expected values, taken from a nominal or reference value. Thus, we quantify changes in the optical wavefront by fitting the measured Zernike coefficients, a_i , to a reference optical wavefront, according to the following expression:

$$a_i(\text{Measured})[x, y] = a_i(\text{Reference})[x, y] + \Delta_i + \Theta_i^x * y + \Theta_i^y * x \quad (3)$$

where x, y are focal plane coordinates, and i is the Zernike index. The reference Zernike coefficients, or reference wavefront map, $a_i(\text{Reference})[x, y]$, are determined from donuts in a single commissioning image, adjusted to yield uniform aberrations close to the expectations from our optical model, as described in more detail in Section 4. Because the reference wavefront map is derived from data, with limited sampling across the focal plane, we utilize a nearest-neighbor interpolation algorithm to return the reference Zernike coefficients at each desired x, y focal-plane location. As an example of this analysis, the difference between the measured wavefront map and the reference map, ΔZ_5 is shown in Figure 6 for the Astigmatism Y term with an ensemble of donuts from a single out-of-focus image taken with a large value of ΔY decenter. The expected linear variation of astigmatism across the focal plane is clearly visible. The residual of ΔZ_5 after the linear fit has a Gaussian distribution, with an RMS of 0.05λ , and provides a convenient means to estimate the actual uncertainty in the wavefront analysis. The analysis of donuts in the wavefront sensors for normal science images proceeds in exactly the same way described here, but of course the Zernike coefficients come only from the eight out-of-focus wavefront CCDs. We perform the linear fit in Equation 3 using a robust fitter to reject outliers, to enhance fault tolerance in the AOS. Typical values for the RMS of the residual distributions from the wavefront sensors are $10\mu\text{m}$ for defocus, 0.08λ for astigmatism, 0.05λ for coma, and 0.04λ for trefoil. With a mean of 30 donuts analyzed in the AOS, the resulting statistical uncertainty from the wavefront analysis is then of order $2\mu\text{m}$ in defocus and below 0.02λ for each aberration.

5.2 Alignment Sensitivity Matrix

For a prime-focus system such as DECam, the hexapod alignment vector \vec{h} is fully determined from the values of Δ_{Coma} and $\Theta_{\text{Astigmatism}}$ found by fitting the appropriate measured wavefront map to its reference map. The information derived from the two astigmatism slopes, $\Theta_{\text{Astigmatism}}$, is redundant, with $\Theta_{Z_5}^x = \Theta_{Z_6}^y$ and $\Theta_{Z_6}^x = -\Theta_{Z_5}^y$; we combine them as $\Theta_x \equiv \frac{1}{2}(\Theta_{Z_5}^x + \Theta_{Z_6}^y)$ and $\Theta_y \equiv \frac{1}{2}(\Theta_{Z_6}^x - \Theta_{Z_5}^y)$. Thus our displacement vector

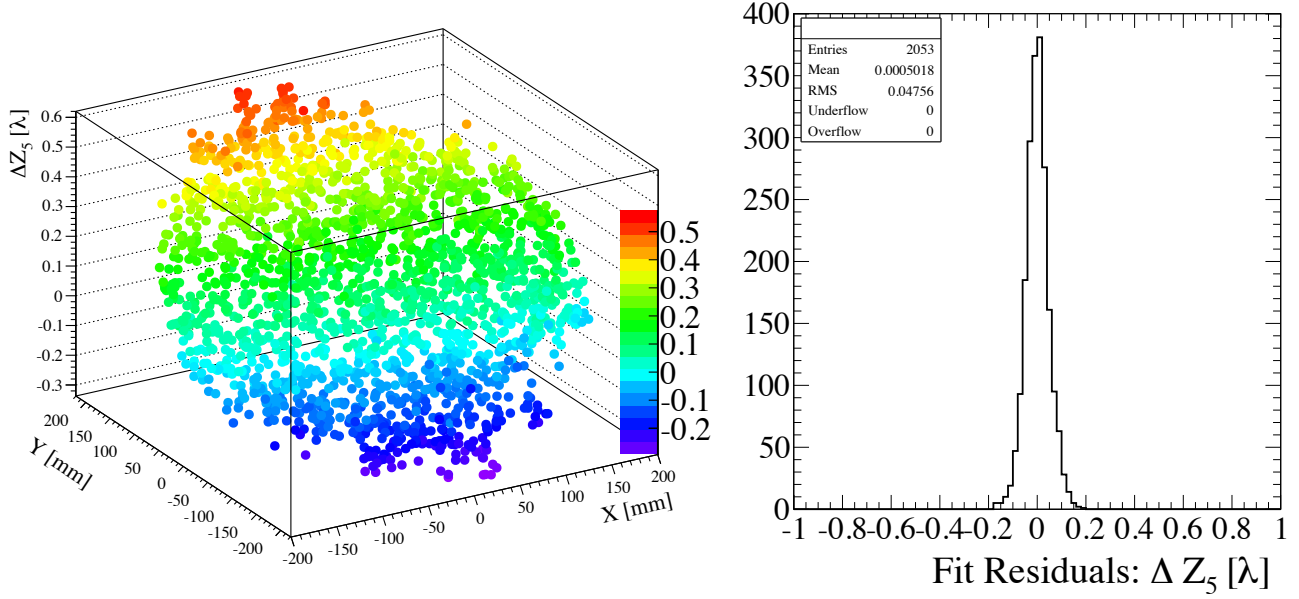


Figure 6. a) The value of the difference between the measured wavefront map and the reference map, $\Delta Z_5 = a_5(\text{Measured})[x, y] - a_5(\text{Reference})[x, y]$, for the coefficient of Astigmatism Y versus focal plane position. Each point represents a single donut observed in one out-of-focus image. This image had the hexapod decentered by 4.5mm . b) The residual of ΔZ_5 after the linear fit. Note that in the robust linear fitting used a few outlier points have been removed.

is given by $\vec{d} = (\Theta_x, \Theta_y, \Delta Z_7, \Delta Z_8)$. The analysis here is equivalent to that expected in a general analysis of wavefront sensitivity,¹² but by separating the analysis into two pieces: a global analysis of each aberration to extract a simple displacement vector and then the application of the matrix relation between alignment and displacement vectors, we have the advantage of including outlier rejection and error analysis in the fit to each wavefront map, and also of having a very simple sensitivity matrix to determine.

The hexapod alignment vector is given by the matrix equation $\vec{h} = \mathcal{S}\vec{d}$, with \mathcal{S} the sensitivity matrix. We determined the sensitivity matrix experimentally by moving the hexapod separately in each degree of freedom and measuring the displacement vector from donuts collected in images taken with DECam placed 1.5mm out-of-focus. The relation between the displacement and alignment vectors is shown in Figure 7, where the measured displacements are shown against each alignment degree of freedom. The linear fits only include the statistical error estimated from the fit to the wavefront maps, and not any systematic component from image-to-image wavefront changes, which are surely present. The expected linear behavior is observed, with slopes which are roughly symmetric under $x \leftrightarrow y$. As expected, half of the slopes are consistent with zero, and we take these as identically zero in the sensitivity matrix. The matrix of slopes $\mathcal{S}^{-1} = \partial\vec{d}/\partial\vec{h}$ from Figure 7 is inverted to yield:

$$\begin{pmatrix} \Delta X[\mu\text{m}] \\ \Delta Y[\mu\text{m}] \\ \theta X[\text{arcsec}] \\ \theta Y[\text{arcsec}] \end{pmatrix} = \begin{pmatrix} 0. & 107000. & 4540. & 0. \\ 118000. & 0. & 0. & -4200 \\ -43600 & 0. & 0. & -82. \\ 0. & 44200. & -81. & 0. \end{pmatrix} \begin{pmatrix} \Theta_x[\lambda/\text{mm}] \\ \Theta_y[\lambda/\text{mm}] \\ \Delta Z_7[\lambda] \\ \Delta Z_8[\lambda] \end{pmatrix} \quad (4)$$

These values compare reasonably well with the expectation from a Zemax model of the Blanco and DECam, except for the $\partial(\Delta X)/\partial(\Theta_y)$ and $\partial(\Delta Y)/\partial(\Theta_x)$ terms which are a factor of two smaller than expected.

5.3 Focus & Alignment Look-Up Tables

The wavefront analysis tools described above are also used to form the alignment look-up tables (LUT), which provides a static correction for the misalignment caused by gravitational flexure of the DECam cage with respect to the primary. A sequence of images was taken, again with DECam out-of-focus by 1.5mm , over a grid of

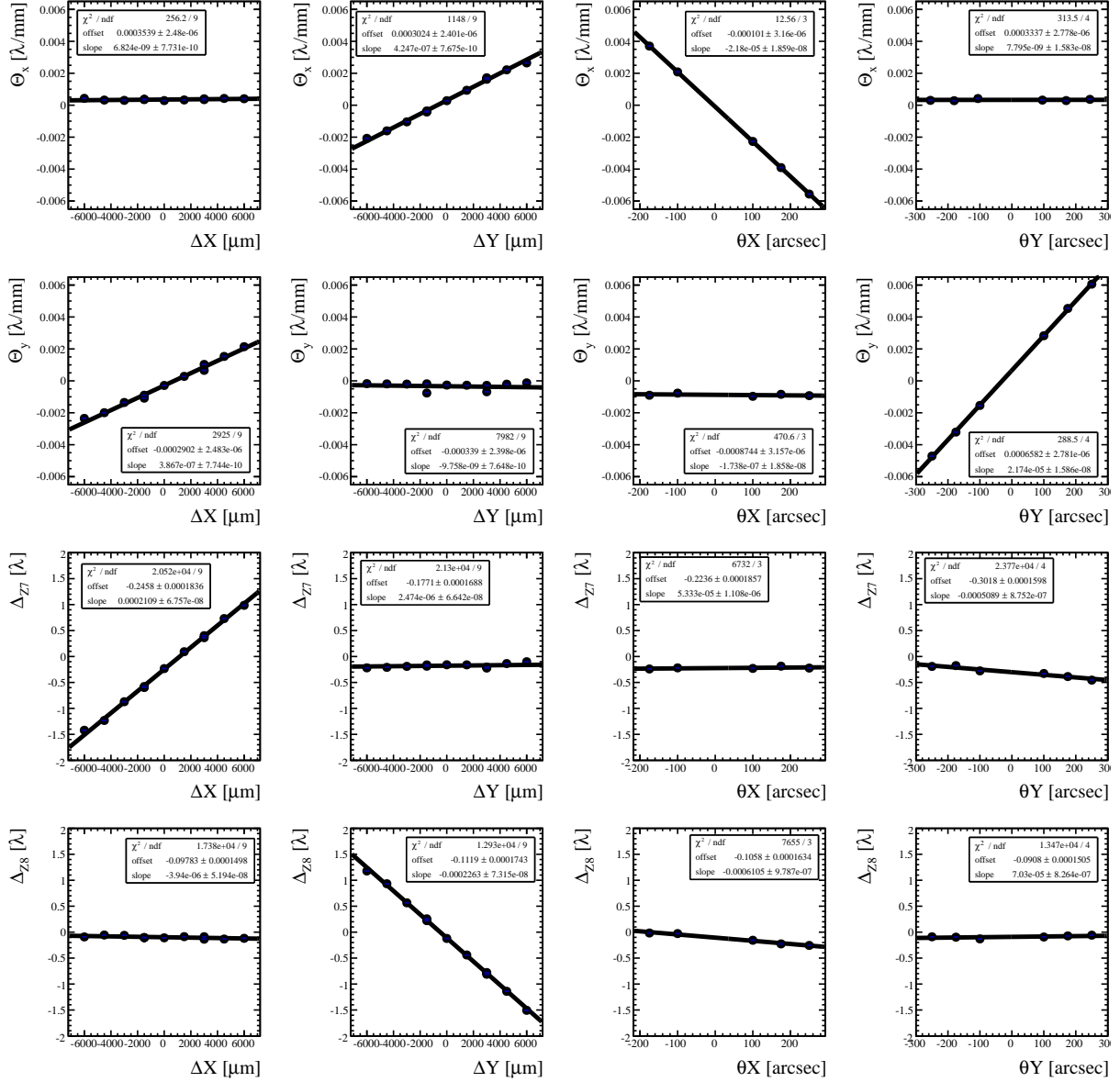


Figure 7. Sensitivity of the displacement degrees of freedom, $\vec{d} = (\Theta_x, \Theta_y, \Delta_{Z7}, \Delta_{Z8})$, on the hexapod alignment degrees of freedom, $\vec{h} = (\Delta X, \Delta Y, \Theta X, \Theta Y)$. Each hexapod degree of freedom is varied independently, and images are collected with the DECcam placed out of focus. The ensemble of donuts are fit and analyzed and the displacement vector determined. Statistical errors are plotted, all smaller than the data points, but a few duplicated points indicate that non-stochastic errors dominate. These fitted slopes are used as elements of the inverse of the sensitivity matrix.

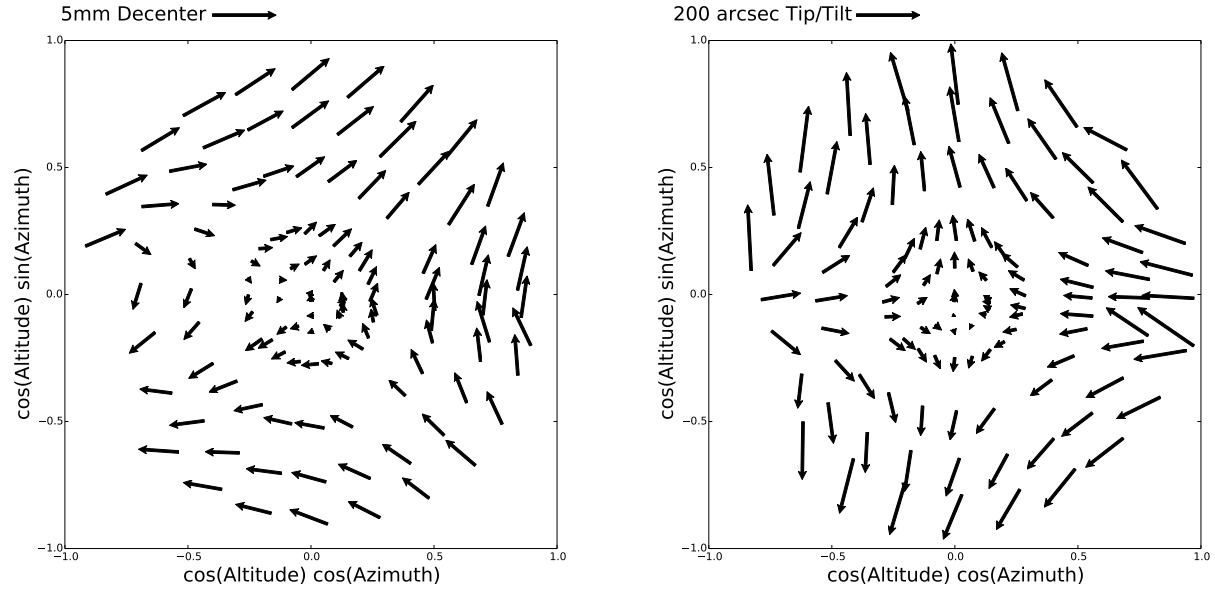


Figure 8. a) Measured decenter ($\Delta X, \Delta Y$) and b) the measured tip/tilt ($\theta X, \theta Y$) vectors, both as a function of telescope altitude and azimuth.

telescope orientations in altitude and azimuth. At each point the ensemble of donuts is fit and their wavefront maps are analyzed, again comparing to the reference wavefront map. Finally, values for the displacement vector are extracted, as shown in Figure 8. This grid of displacement vectors was used to populate the alignment LUT. DECam also has a laser tracking system,¹³ which provided an independent check of the LUT, and was used to smooth the LUT values. The scan in orientation used to create the LUT was repeated on several occasions; the results were qualitatively quite similar, but systematic differences in the magnitude of the flexure were observed between images taken several months apart. Whether this was due to hysteresis in the flexure, temperature variations, or some other effect is not known. However, the AOS acts to bring the alignment to a fixed optical set-point, even with systematic offsets in the LUT. In addition, there is a focus LUT indexed by telescope orientation and built in the same way as the alignment LUT, which captures small variations in focus. Lastly, there is a table of focus offsets for each filter.

6. DECAM AOS OPERATION

The AOS was commissioned in the fall of 2012, together with DECam as a whole. The AOS established unsupervised control of focus, with the LUT in place for the other hexapod degrees of freedom, at the end of the commissioning period. DECam commissioning was followed by several months of science verification; during this period the AOS began operation with unsupervised control of the hexapod alignment as well. At the end of the science verification period the AOS was routinely operated in fully unsupervised control of focus and alignment for both DES and community observing. The AOS has continued to operate successfully in this mode, with essentially no observer setup or intervention required.

The AOS has fault tolerance built into every step of analysis and control. A requirement on the shape of the donuts remove overlapping stars at the selection stage. Many remaining overlaps as well as poor Zernike fits are removed by demanding reasonable values of the Zernike coefficients. Next the fit of the reference wavefront map to the fitted wavefront map is performed as a robust linear fit, where outliers are de-weighted. Any remaining overlapping stars, or other fitting problems, are generally removed by this stage. Donuts with outliers in one Zernike term are also removed from the fit in the other Zernike terms. We require that at least 5 donuts remain after all these requirements, and demand that the estimated error on the focus and hexapod displacements be

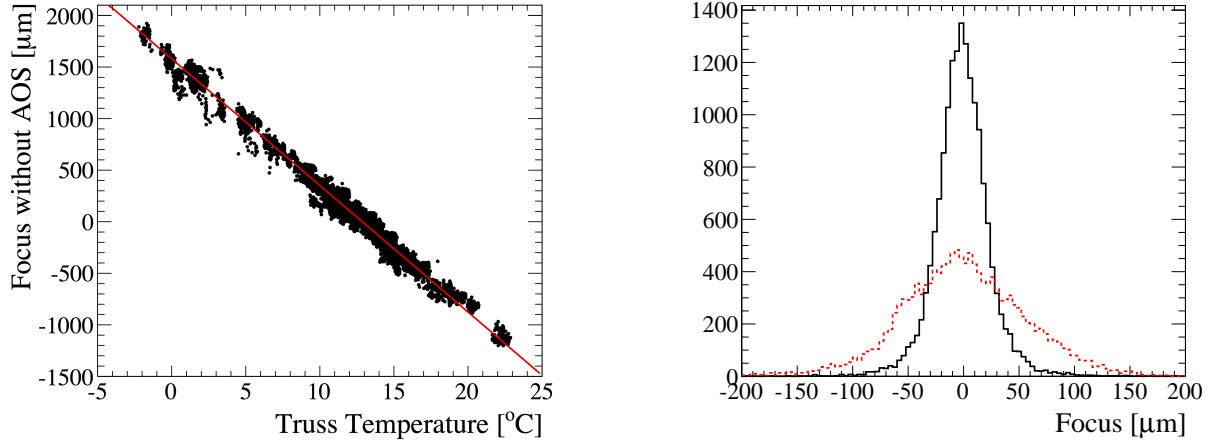


Figure 9. a) Distance from nominal focus, with only the focus LUT, vs. truss temperature. The slope of these points indicate a change in focus of $120\mu\text{m}/^{\circ}\text{C}$. b) Distance from nominal focus for the AOS (black, solid line) and for a linear temperature correction (red, dotted line). Images from the DES year 1 wide-field survey are used in these plots. The focus RMS for the AOS is $24\mu\text{m}$, compared to $60\mu\text{m}$ for a linear temperature correction.

reasonable. Next the PID control loop, with proportional coefficients of 0.3, integral of 0.12 and derivative of 0.188, acts to damp out noise, from whatever source. Finally, we limit the absolute size of hexapod adjustments from the AOS for any single image to be less than $200\mu\text{m}$ in focus, $250\mu\text{m}$ in decenter, and 40 arcsec in tilt.

DECam focus is linearly dependent on the temperature of the truss supporting the prime focus cage. We can see this in Figure 9 which shows the distance from focus without the AOS, or any temperature dependent correction, versus the truss temperature. The previous prime focus instrument at the Blanco, the MosaicII, relied on a linear truss temperature focus correction, with a very similar slope to that observed with DECam. With just a temperature correction, DECam would have had a $60\mu\text{m}$ RMS deviation from best focus, while with the AOS we achieve a focus RMS of $24\mu\text{m}$, as shown in Figure 9. As an example of AOS operation, a time history of the LUT value, AOS adjustment and resulting measured distance to nominal focus is shown in Figure 10 for a typical night of DES observing. Also we show in Figure 11 the distributions of measured decenter and tilt from the AOS, compared with those from just the LUT alone. While the improvement in the RMS of these distributions from the AOS are more modest, the AOS ensures that DECam stays centered around the nominal alignment. We have also studied the behavior of the AOS as a function of the size of the telescope slew made prior to each image. Recall that we keep a running tally of the AOS corrections to the focus and alignment, even after large telescope slews. We do find that the AOS performs better after small slews than large ones, however the AOS does yield some improvement even after large slews. We note that the systematic offset of the LUT-only values in ΘX and ΘY may be due to the hysteresis effects noted above. The AOS yields control of the hexapod alignment degrees of freedom at a level of 250 and $290\mu\text{m}$ RMS for decenter and 11arcsec RMS for tilt. We note that the AOS control level is noticeably larger than the typical statistical uncertainty of $2\mu\text{m}$ in focus, $35\mu\text{m}$ in decenter, and 3arcsec in tilt. One possible source of this discrepancy is systematic errors in the Zernike fits, perhaps from omitting higher order aberrations. However, we tend to discount this source since it would have to cause a uniform change in the Zernike coefficients, even though the donuts vary greatly across the focal plane. There is some evidence that the excess spread in hexapod alignment is due to image to image wavefront error, since this level of focus or aberration noise is even observed for successive images taken at the same point on the sky. Such wavefront error could be due to mirror, dome or ground layer seeing, or perhaps to hysteresis or control errors in the Blanco primary mirror airpad supports. The spread in the AOS focus is somewhat smaller for periods with good seeing and image quality, which points to seeing induced wavefront changes as a possible source.

We can use the ensemble of images taken with DECam to explore the set-point of the AOS; whether we

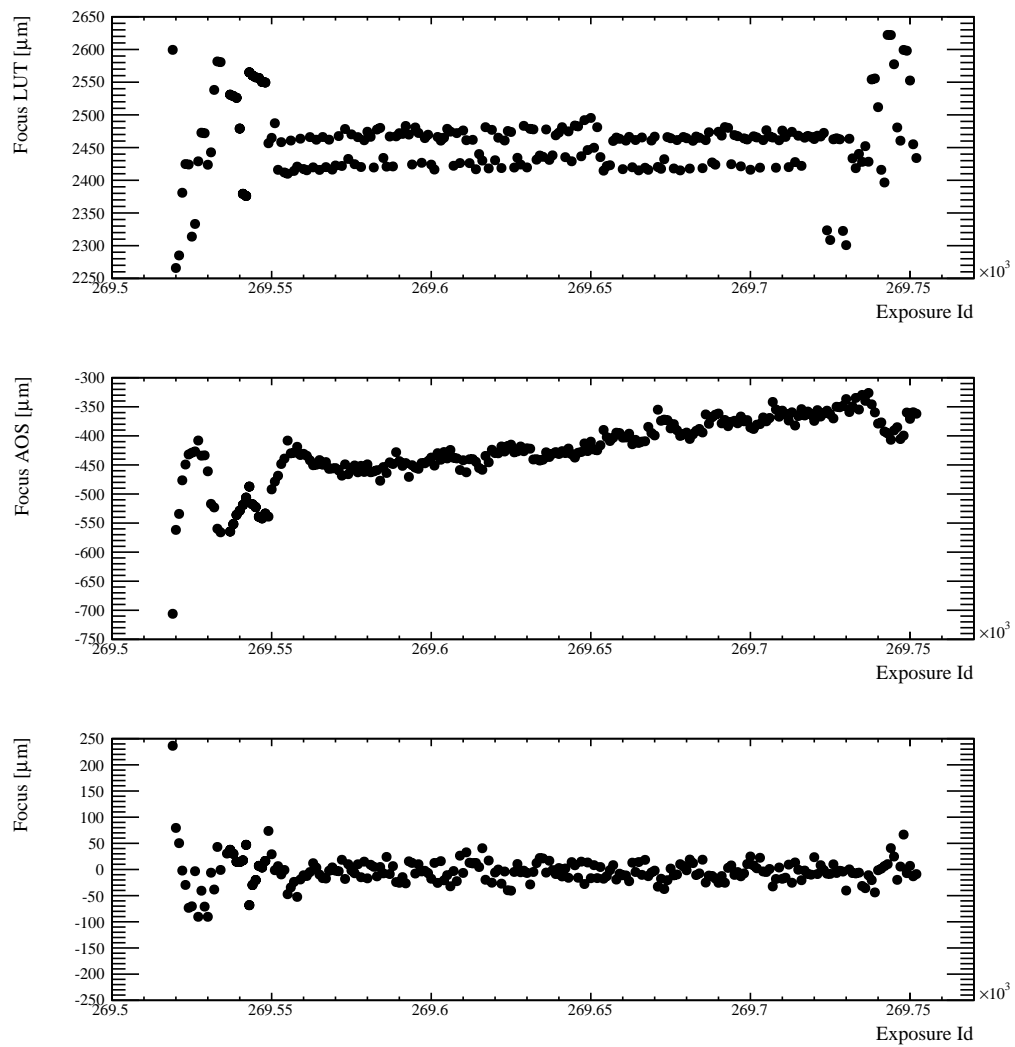


Figure 10. a) LUT value for focus vs. exposure number for a typical night of DES observing. The LUT for focus is indexed by altitude and azimuth as well as by filter; the focus offset between different filters is plainly visible b) AOS adjustment to focus vs. exposure number and c) Measured distance to nominal focus vs. exposure number.

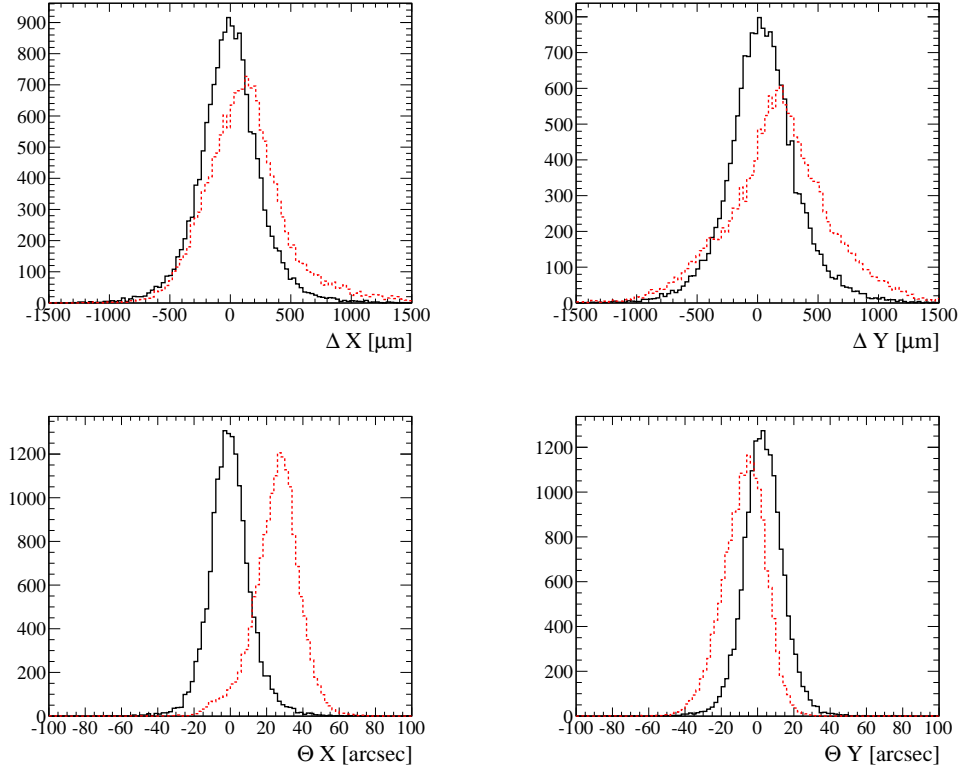


Figure 11. The hexapod alignment degrees of freedom, showing the distance from nominal decenter or tilt for the AOS (black, solid line) compared to the LUT only (red, dotted line) for a) ΔX , b) ΔY , c) θX , d) θY .

are actually setting the focus and alignment to their optimal values. However, the wide distribution of seeing conditions makes it difficult to use image quality alone for such studies. Better is to use the difference between delivered image quality and seeing. CTIO has a DIMM seeing monitor, but there is evidence that mirror or dome seeing can be significant, which are not captured by the DIMM measurements. Instead we have been able to extract a smearing measurement, including all forms of seeing as well as CCD diffusion and jitter, from the donuts themselves. Our normal donut fit fixes the width of the smearing kernel, but offline we can optionally include the smearing width as an additional floating parameter. In particular the steepness of the donut edges are sensitive to all sources of image smearing. We show in Figure 12 the mean FWHM from stars versus the donut derived smearing, demonstrating that this method for extracting the image smearing does work well. Next we compare the difference between the FWHM and the image smearing against the measured distance from nominal focus, in Figure 13. The resulting distribution shows that the nominal focus is indeed nearly optimal. Similar plots for the other alignment degrees of freedom have much less distinct minima, and while the nominal alignment positions appear to be close to optimal further improvement may be possible.

7. BLANCO PRIMARY MIRROR WAVEFRONT

The Blanco's 4-meter primary mirror is supported by an array of airpads,¹⁴ whose pressure is adjusted to optimize the mirror figure. The sensitivity to the primary mirror figure was tested by taking engineering images with the airpads set to produce an induced astigmatism and then we measured the astigmatism with the machinery described above. A comparison of the magnitude of the astigmatism, defined as $\sqrt{a_5^2 + a_6^2}$, is shown in Figure 14. There is reasonable agreement between the input and measured astigmatism, although repeated images taken with the same conditions do show changes in astigmatism of up to 0.1λ , which may be due to the same systematic

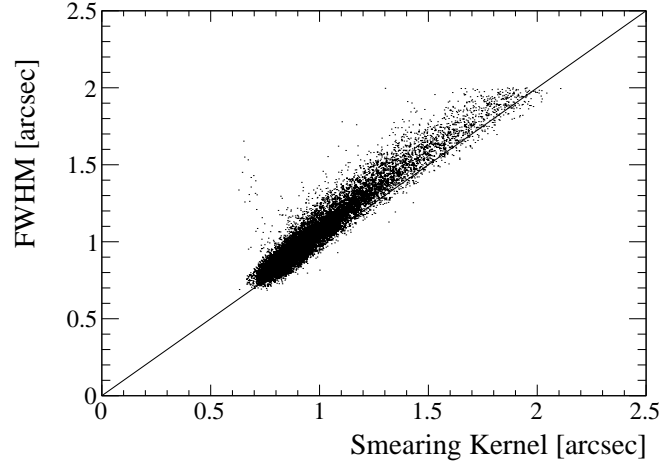


Figure 12. The mean FWHM from stars versus the donut measured smearing. The line plotted has a slope of one.

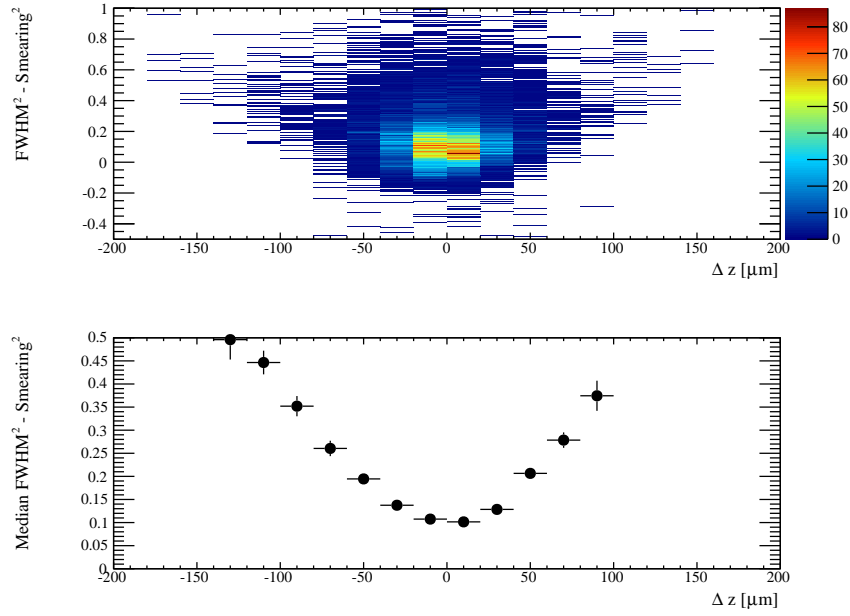


Figure 13. FWHM minus donut measured smearing, in quadrature, versus the measured distance from nominal: a) is a two-dimensional histogram and b) is the Median FWHM minus smearing vs. Δz . We do not take the square root of the difference between FWHM and smearing, since some of the entries are negative. DES images taken in r, i, z and Y filters from both the science verification period and year one are included.

effects discussed in the context of the AOS. Given this and the possibility that there may be sources of hysteresis in the control of the Blanco's primary mirror figure, this topic will be the subject of continued study.

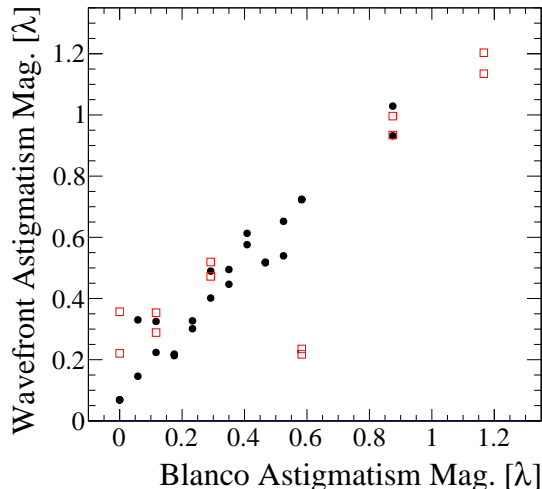


Figure 14. The measured magnitude of the astigmatism versus the astigmatism introduced into the primary mirror. The induced astigmatism was first increased monotonically (black circles), and then decreased monotonically (red open squares). The first set of points is reasonably linear, but the second set does not return to the original astigmatism value, indicating that some hysteresis may be present in the airpad control system. (The points off the line at an input astigmatism at 0.6 may have had an operational problem with the airpad system)

8. DECAM WAVEFRONT AND POINT SPREAD FUNCTION

The maps of Zernike coefficients should provide a complete description of the optical wavefront of the Blanco and DECam system, and in the limit that the seeing, CCD diffusion and telescope tracking jitter are uniform across the focal plane, this information should also completely describe the variation of the observed point spread function (PSF). Thus we aim to describe the PSF, from stars across the focal plane, with our information about the optical wavefront plus a few additional parameters to encompass seeing and other sources of smearing of the PSF. The latter is our wavefront-based model, it consists of the Zernike coefficient wavefront maps, now expanded to include the spherical aberration, plus a numerical convolution of a seeing and pixelization kernel. Since seeing dominates over CCD diffusion and tracking jitter our model of the smearing as the Fourier transform of the Kolmogorov spectrum is a reasonable approximation. In practice we use the same computational engine as used to calculate donut images; with a small focus aberration we yield a model of in-focus stars instead of donuts. Note that the wavefront model is numerical, it produces pixelized images.

To connect the PSF and the wavefront-based model, we characterize the PSF in terms of low-order moments, and compare them to the same moments calculated from simulated stars generated by the model. Second moments yield information proportional to FWHM and ellipticity. The distinctive trefoil pattern pushes us to also include third order moments, which are sensitive to coma and trefoil. We add a limited set of free parameters to the wavefront model, these include the width of the smearing kernel, two parameters to account for tracking jitter, plus offsets and slopes for each of the Zernike terms. These offsets and slopes generally correspond to the physical degrees of freedom, in the alignment and primary mirror figure, which may impact at lowest order each Zernike term. Thus we add free parameters Δ_i and $\Theta_i^{x,y}$ for each term, which modifies the Zernike coefficient as:

$$a_i[x, y] = a_i(\text{Reference})[x, y] + \Delta_i + \Theta_i^x * y + \Theta_i^y * x \quad (5)$$

If the alignment and mirror figure were both perfectly stable, the Δ_i and Θ_i should be equal to zero, or equal to a constant should the $a_i(\text{Reference})[x, y]$ be systematically offset from the AOS set-points. The latter case could

occur if there were a registration offset between wavefront maps used in the AOS and those used for the PSF wavefront model.

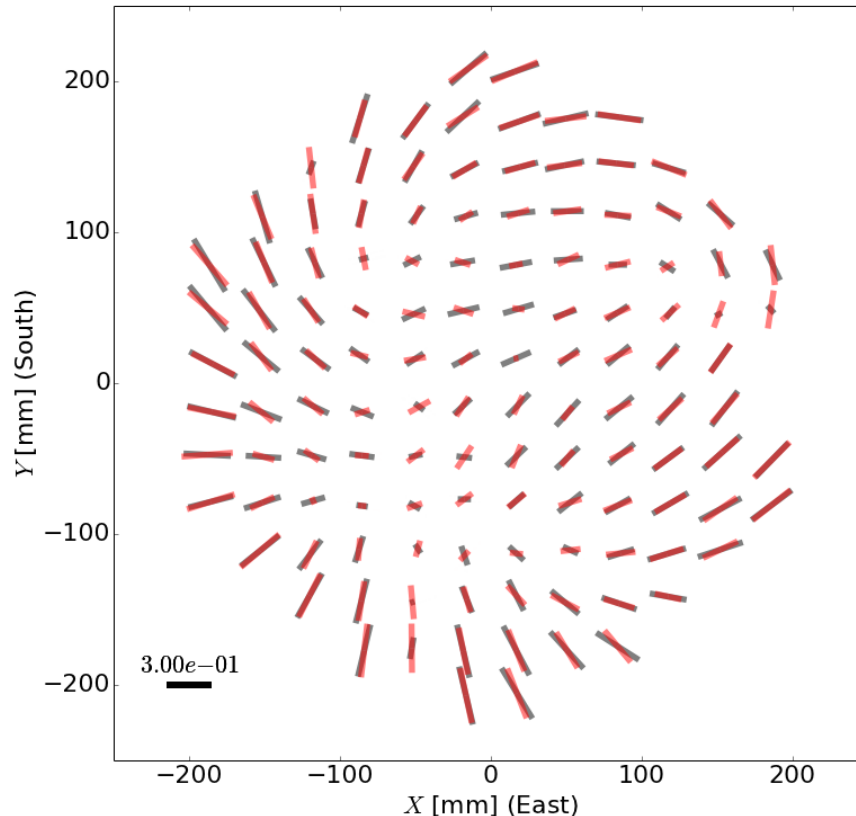


Figure 15. The whisker pattern as a function of focal plane coordinate from a single DES image. The data, measured from selected stars, is shown in black, while the wavefront-based model is shown in red. Whisker is defined with a magnitude given by $w = [(I_{xx} - I_{yy})^2 + (2I_{xy})^2]^{1/4}$, and the scale bar has a whisker of $0.3arcsec$.

We proceed by fitting the PSF moments of selected stars from single images to the wavefront model. The ellipticity across the focal plane, from a single image, after such a fit is shown in Figure 15. Here the magnitude of the whiskers are defined as $w = [(I_{xx} - I_{yy})^2 + (2I_{xy})^2]^{1/4}$. Note that the fit uses only 20 free parameters for the entire focal plane, but yields a good match to much of the whisker pattern observed. A further test of the wavefront model is made in Figure 16 where we compare the results of the fit against values for the equivalent parameter from the AOS. Excellent linear correlation between results of the wavefront model fit to the PSF is observed compared to the AOS values, albeit with a non-zero offset between the two. Further study of this offset should inform our determination of whether the AOS alignment set-points are indeed optimal. While these are preliminary results from the wavefront-based fits, our ultimate goal is to characterize the PSF with this method as part of a weak lensing pipeline for DES.

9. CONCLUSIONS

We have presented a detailed description of the DECam wavefront retrieval algorithm, the optical wavefront characterization, the AOS design, calibration and operation during the first year of DES data. The AOS is in

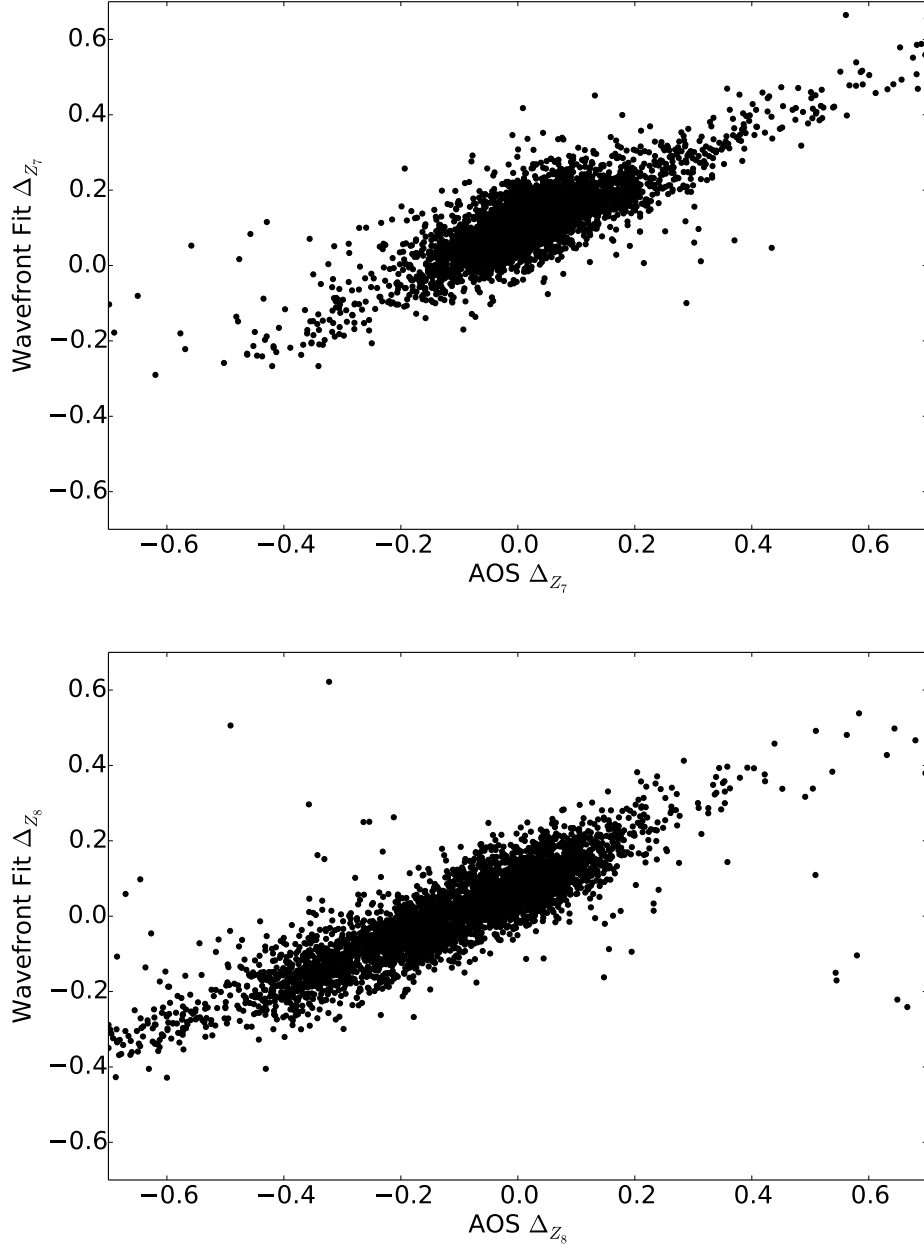


Figure 16. Results from the fit to stellar moments with the wavefront model, comparing the value of the Coma offsets in the wavefront fit against the equivalent quantity from the AOS. a) ΔZ_7 b) ΔZ_8

routine operation with DECam, and we anticipate no significant changes to its operation, except for modest adjustments of the LUT or AOS set-points. Finally we also presented preliminary results on fits to moments of the PSF using a wavefront model which fits individual images with a small number of free parameters.

Acknowledgements

This work was supported by the U.S. Department of Energy under contract number DE-AC02-76-SF00515. In addition to our DES and CTIO colleagues, we would especially like to thank Alistair Walker, Roberto Tighe,

Steve Kent, Klaus Honscheid, Gary Bernstein, David Gerdes, Adam Sypniewski, David Burke and Paul Schechter for numerous useful discussions.

REFERENCES

1. B. L. Flaugher *et al.*, “Status of the Dark Energy Survey Camera (DECam) project,” in *Ground-based and Airborne Instrumentation for Astronomy IV. Proceedings of the SPIE*, pp. 844611–844611–15, Sept. 2012.
2. T. Abbott *et al.*, “The Dark Energy Survey,” *astro-ph/0510346*, 2005.
3. A. Roodman, “Focus and alignment of the Dark Energy Camera using out-of-focus stars,” in *Ground-based and Airborne Instrumentation for Astronomy IV. Proceedings of the SPIE*, **8446**, Sept. 2012.
4. A. Roodman, “Focus and alignment using out-of-focus stellar images at the dark energy camera,” in *Ground-based and Airborne Instrumentation for Astronomy III. Proceedings of the SPIE*, **7735**, 2010.
5. E. Bertin and S. Arnouts, “SExtractor: Software for source extraction,” *A&AS* **117**, pp. 393–404, June 1996.
6. J. R. Fienup, “Phase-retrieval algorithms for a complicated optical system,” *Applied Optics (ISSN 0003-6935)* **32**, p. 1737, Apr. 1993.
7. A. Tokovinin and S. Heathcote, “Donut: Measuring optical aberrations from a single extrafocal image,” *The Publications of the Astronomical Society of the Pacific* **118**, p. 1165, Aug 2006.
8. C. Roddier and F. Roddier, “Wave-front reconstruction from defocused images and the testing of ground-based optical telescopes,” *Journal of the Optical Society of America A* **10**, pp. 2277–2287, Nov. 1993.
9. R. J. Noll, “Zernike polynomials and atmospheric turbulence,” *J. Opt. Soc. America* **66**, p. 207, Jan 1976.
10. F. James and M. Roos, “Minuit - a system for function minimization and analysis of the parameter errors and correlations,” *Computer Physics Communications* **10**, pp. 343–367, 1975.
11. P. Doel *et al.*, “Design and status of the optical corrector for the DES survey instrument,” *Ground-based and Airborne Instrumentation for Astronomy II. Edited by McLean* **7014**, pp. 63–70141V–11, Aug. 2008.
12. P. L. Schechter and R. S. Levinson, “Generic Misalignment Aberration Patterns in Wide-Field Telescopes,” *Publications of the Astronomical Society of the Pacific* **123**, pp. 812–832, July 2011.
13. A. Sypniewski, *Optimizing Photometric Redshift Estimation for Large Astronomical Surveys Using Boosted Decision Trees*. PhD thesis, University of Michigan, 2014.
14. G. Schumacher, J. Baldwin, G. Perez, and E. Mondaca, “Active optics system for the CTIO 4-m telescope,” *Proc. SPIE Vol. 2479* **2479**, pp. 389–398, June 1995.